

Air-water interaction and characteristics in breaking bores

Xinqian LENG (¹) and Hubert CHANSON (¹) (*)

(¹) The University of Queensland, School of Civil Engineering, Brisbane QLD 4072, Australia

(*) Corresponding author: h.chanson@uq.edu.au, (61 7) 3365 3516

ORCID numbers

Xinqian LENG: 0000-0001-8472-7925

Hubert CHANSON: 0000-0002-2016-9650

Abstract

A tidal bore is an unsteady rapidly-varied open channel flow characterised by a rise in water surface elevation in estuarine zones, under spring tidal conditions. After formation, the bore is traditionally analysed as a hydraulic jump in translation and its leading edge is characterised by a breaking roller for Froude number $Fr_1 > 1.3$ -1.5. The roller is a key flow feature characterised by intense turbulence and air bubble entrainment. Detailed unsteady air-water flow measurements were conducted in a breaking bore propagating in a large-size channel, using an array of three dual-tip phase detection probes and photographic camera. The data showed a relatively steep roller, with a short and dynamic bubbly flow region. Air entrainment took place in the form of air entrapment at the roller toe, air-water exchange across the roller 'free-surface', spray and splashing with dynamic water drop ejection and re-attachment, roll up and roll down of water 'tongues' engulfing air pockets. The roller free-surface profile and characteristics were comparable to observations in stationary hydraulic jumps and steady breaker, for similar flow conditions. Within the roller, the amount of entrained air was quantitatively small for Froude number $Fr_1 = 2.2$. The number of air bubbles was limited, with between 5 to 20 bubbles per phase-detection probe sensor detected at each vertical elevation. The entrained air bubble chord lengths spanned over several orders of magnitude, with a large proportion of clustered bubbles. Overall, the study highlighted the three-dimensional nature of the air-water roller motion and strong evidence of the in-homogeneity of the turbulent air-water mixture.

Keywords

Unsteady flow; aerated flow; two-phase air-water flow; breaking bore; physical modelling

1. Introduction

A tidal bore is a series of waves propagating upstream as the tidal flow turns to rising in a river mouth during the early flood tide. The shape of the bore is closely linked to its Froude number Fr_1 . Breaking bores occur for $Fr_1 > 1.5$ to 1.8. A key feature of breaking bores is the rapid spatial and temporal deformations of the roller free-surface in response to interactions between entrained air bubbles and turbulent structures (KOCH and CHANSON 2009, LENG and CHANSON 2015a) (Fig. 1). The effects of air entrainment on breaking wave impact were documented in laboratory and in the field (PEREGRINE 2003). It was shown that the entrapped air can be compressed, and resulting pressure shock waves can contribute to some substantial impact on structures (BREDMOSE et al. 2009). The air entrainment in breaking bores has not been investigated to date, except for a few preliminary works (CHANSON 2009a,2010,2016b, LENG and CHANSON 2015a), and a limited analogy with stationary hydraulic jumps (CHANSON 2009b, WANG et al. 2017). CHANSON (2009a,2016b) studied the atmospheric noise of breaking tidal bores, linking the low pitch sound of the advancing bore to a dominant frequency of collective oscillations of bubble clouds in the bore roller. CHANSON (2010) documented underwater bubble acoustic beneath a breaking bores, while LENG and CHANSON (2015a) performed phase-detection probe measurements in breaking bore rollers.



Fig. 1 - Breaking tidal bore of the Qiantang River at Qilimiao (China) on 11 October 2014 at 13:20 - Bore propagation from left to right, viewed from left bank - The roller height was between 2 m to 3 m and the bore was 2.7 km wide

Herein physical investigations were conducted in laboratory with a focus on the microscopic air-water flow properties in the breaking bore roller. New experiments were conducted in a

large size facility. The study focused on unsteady air entrainment measurements in the bore roller using an array of phase-detection probes, with high-resolution high-shutter-speed photographic observations on the side. Air-water properties were investigated in details by applying instantaneous and ensemble-averaged experimental techniques, including the first data set on liquid fractions, void fractions, aerated roller characteristics and bubble clustering in breaking bores and travelling hydraulic jumps.

2. Experimental facility, instrumentation and flow conditions

The experimental facility was a large rectangular channel, with a 19 m long and 0.7 m wide test section and an adjustable channel slope. The test section was made of glass side walls and smooth PVC bed. The same channel was previously used by LENG and CHANSON (2015a,2016). The initially steady flow was supplied by an upstream intake tank equipped with flow calming devices and flow straighteners, leading to the 19 m long glass-sidewall test section through a smooth three-dimensional convergent. A fast-closing Tainter gate was located next to the downstream end of the channel at $x = 18.1$ m, where x is measured from the upstream end of the channel. The bore was generated by rapidly closing the Tainter gate and the bore propagated upstream (Fig. 2). The gate closure time was less than 0.2 s and did not affect the upstream bore propagation. The Tainter gate was identical to that previously used by and described in LENG and CHANSON (2015a,2016). Figure 2 presents an overview of the experimental channel and facility setup.

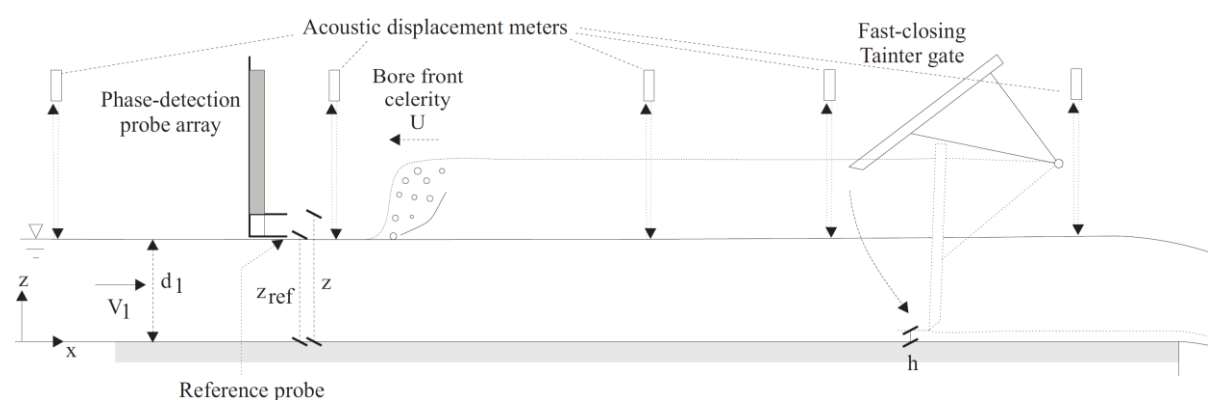


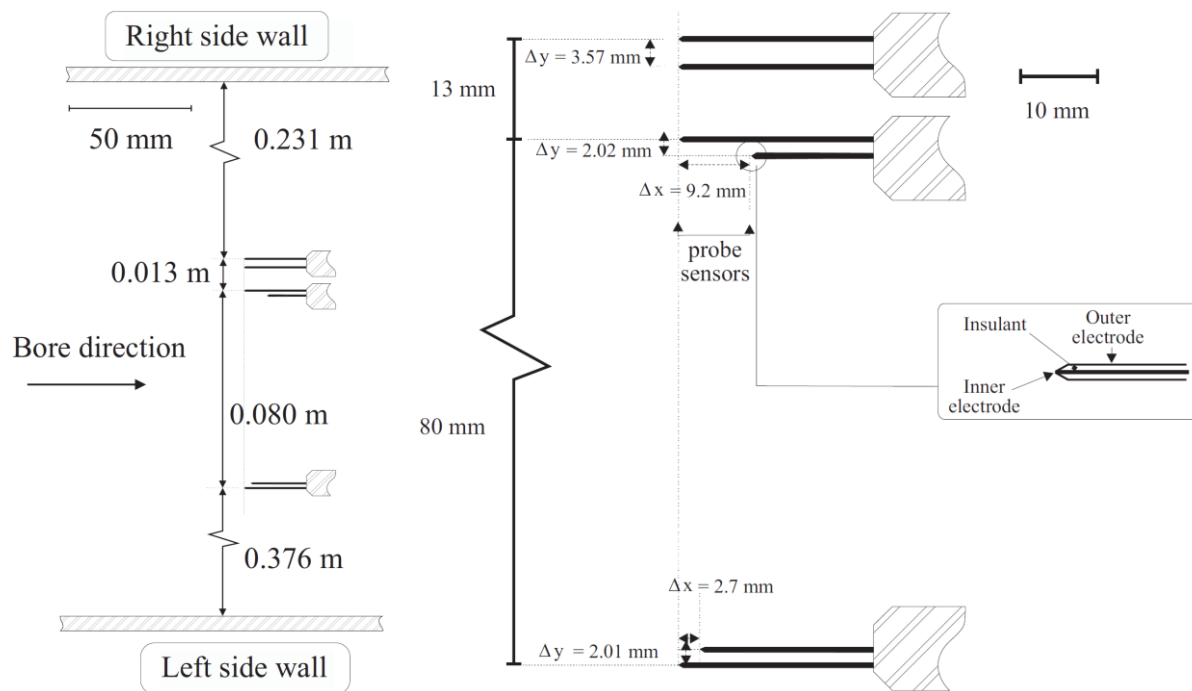
Fig. 2 - Sketch of the experimental facility - Distorted scales

The discharge was measured by a magneto flow meter with an accuracy of 10^{-5} m³/s. In steady flows, the water depths were measured using point gauges, with an accuracy of 0.001 m. The unsteady water depths were recorded with a series of acoustic displacement meters (ADMs).

A Microsonic™ Mic+35/IU/TC unit was located at $x = 18.17$ m immediately downstream of the Tainter gate. Four acoustic displacement meters Microsonic™ Mic+25/IU/TC were spaced along the channel between $x = 17.41$ m, 9.96 m, 8.50 m, 6.96 m, upstream of the Tainter gate. All acoustic displacement meters (ADMs) were calibrated against point gauge measurements in steady flows and the sensors were sampled at 20 kHz.

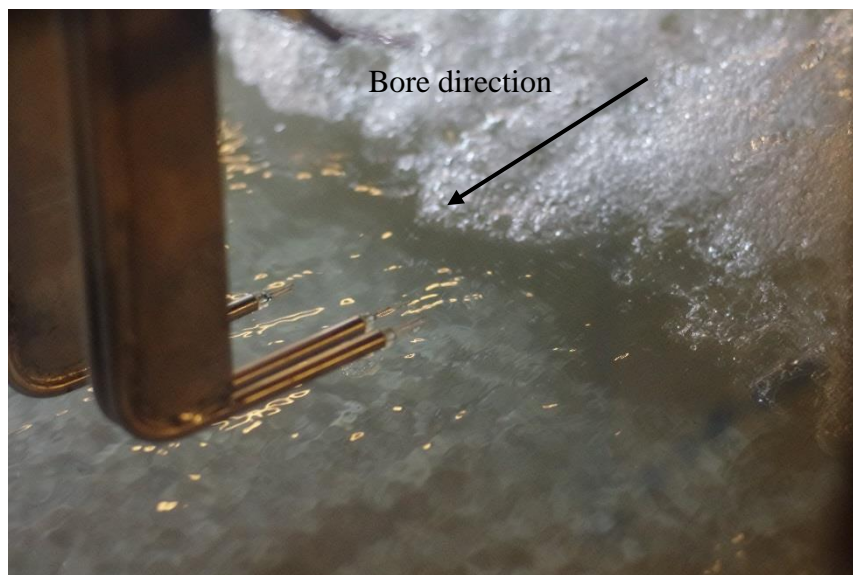
The air-water flow properties were recorded using an array of three dual-tip phase-detection probes located at $x = 8.50$ m. That is, the leading sensor of each probe was located at $x = 8.50$ m.. Each dual-tip probe was equipped with two needle sensors developed at the University of Queensland. Each needle sensor consisted of a silver wire ($\varnothing = 0.25$ mm) insulated from the outer needle. The inner electrode ($\varnothing = 0.25$ mm) was made of silver (99.99% purity), with some $24\text{ }\mu\text{m}$ PTFE insulation coating. The outer electrode was a stainless steel hypodermic needle (304 stainless steel, ID=0.5mm, OD=0.8 mm). The two tips were mounted on a $\varnothing 8$ mm tube housing the connectors and cables. Figure 3 presents some details of the probe arrangement. One probe (Probe 2) was equipped with two identical sensors separated transversally by $\Delta y = 0.0037$ m. The other two probes were equipped a leading and trailing sensor, separated longitudinally by $\Delta x = 0.0027$ m and 0.0092 m. One probe, located about the channel centreline (Fig. 3A, lowest probe), was used as a reference, using the same approach as CHANSON (2004b,2005) in a dam break wave. Its position remained unchanged for the entire duration of the experiments. The other probe (Probe 1) was placed at the same vertical elevation as Probe 2, and its leading sensor was at the same longitudinal position (and vertical elevation) as the sensors of Probe 2. All sensors were aligned with the longitudinal direction, facing downstream and designed to pierce the bubbles/droplets in the bore roller. The probe sensors were excited simultaneously by an electronic system (Ref. UQ82.518) designed with a response time less than $10\text{ }\mu\text{s}$. The sampling rate was 20 kHz or 100 kHz per sensor for all probes. Figure 3 shows the probe array arrangement for experiment series 1, 2 and 3. Flow conditions of the series are listed in Table 1.

High-resolution photographs were taken with a dSLR camera Pentax™ K-3 (6016×4000 pixels). The camera was equipped either with a macro lens Voigtlander™ APO-Lanthar 125mm f/2.5 SL, producing images with an absolutely negligible degree ($\sim 0.44\%$) of barrel distortion, or a lens Voigtlander™ Nokton 58 mm f/1.4 SL II, producing images with insignificant degree ($\sim 0.31\%$) of barrel distortion. The camera operated in shutter-priority mode. The shutter speed was set between $1/320$ s to $1/8,000$ s, corresponding to an exposure time between 3.1 ms and $125\text{ }\mu\text{s}$ respectively.



(A, Left) Dimensioned sketch viewed in elevation - Initially steady flow direction from right to left, bore propagation from left to right - Right: details of the probe sensor locations

(B, Right) Dimensioned sketch of probe arrangement details (view in elevation)



(C) High-speed photograph (shutter speed: 1/2,000 s) of probe array immediately before roller impact, bore propagation from top right to bottom left

Fig. 3 - Details of the phase-detection probe array (experiment series 1, 2 and 3)

LENG, X., and CHANSON, H. (2019). "Air-Water Interaction and Characteristics in Breaking Bores." *International Journal of Multiphase Flow*, Vol. 120, Paper 103101, 17 pages (DOI: 10.1016/j.ijmultiphaseflow.2019.103101) (ISSN 0301-9322).

Table 1 - Experimental flow conditions for air-water flow measurements in breaking bore (Present study)

Experiment	Q m/s	S _o	d ₁ m	U m/s	Fr ₁	Reference probe z _{ref} m	Probe array z m	Instrumentation	Comment
Series 1	0.101	0.0075	0.097	0.64	2.18	0.105	0.095 to 0.255	Acoustic displacement meters, array of phase-detection probes (20 kHz sampling)	Single run for each elevation. Total: 33 elevations. All probes located at x = 8.5 m.
Series 2	0.101	0.0075	0.097	0.64	2.18	0.105	0.105, 0.110, 0.120, 0.145, 0.175, 0.205	Combination of 3 dual-tip phase-detection probes (100 kHz sampling), Phantom ultra-high-speed camera v2011 (22,000 fps)	5 runs for each elevation. All probes located at x = 8.5 m.
Series 3	0.101	0.0075	0.097	0.64	2.18	0.105	0.120, 0.175	Combination of 3 dual-tip phase-detection probes (100 kHz sampling),	25 runs for each elevation. All probes located at x = 8.5 m.

Notes: d₁: initial water depth measured at x = 8.5 m; Fr₁: bore Froude number recorded at x = 8.5 m; Q: initially steady water discharge; U: bore celerity positive upstream; z: probe elevation above the bed; z_{ref}: reference probe elevation above the bed; Probe array: array of Probe 1 and Probe

3. Experimental Results

3.1 Air-water flow patterns

A breaking bore was characterised by its marked roller. Key features of the breaking bore roller included the spray and splashing ahead and above the roller, air bubble entrainment at the roller toe and through the roller's upper free-surface, and rapid fluctuations in space and time of the roller shape and form (Fig. 4). Figure 4 shows a typical instantaneous side view of the bore roller, propagating from left to right in the photograph. In front of the roller, the free-surface was flat and parallel to the channel invert. Upstream of the roller toe, the flow was un-disturbed. It became strongly turbulent downstream of (i.e. behind) the impingement point with large vertical fluctuations and a bubbly/foamy region of large-scale turbulence, i.e. the roller. Air entrainment took place in the form of air entrapment at the roller toe, air-water exchange across the roller 'free-surface', spray and splashing with dynamic water drop ejection and re-attachment, roll up and roll down of water 'tongues' engulfing air pockets. In the roller, large and rapid amplitude motions and strong fluctuations in time and space took place, as evidenced by high-shutter speed photography (Figs. 4 & 5A).

The observations showed the presence of water filaments and droplets ejected in front of the roller (Figs. 4 & 5A). Figure 4 (arrow) shows the onset of droplet ejection ahead of the roller and Figure 5A presents a detailed example. Similar observations of droplet ejections were seen in the breaking bore of the Qiantang River (China) by the authors on 23 September 2016, at the Qiantang river Bore Observation Station (QBOS), Yanguan (China). In the Qiantang River bore, water droplets could be ejected up to 1 m to 1.5 m ahead of the roller toe.

The roller front consisted of foamy mixtures and complicated air-water flow structures. Figure 5B and 5C present typical examples. Air-water flow structures constantly evolved in shape and size, in response to the turbulent fluctuations and interactions with the roller and free-surface. High-resolution photographs showed large air-water structures similar to the one seen in Figure 5C. Such air-water structures were seen to be ejected upwards in all directions (upstream, downstream, upwards, sideways) and to re-attach the roller, either by gravity, re-attachment to another structure or by being caught up by some overturning motion. Other air-water structures resulted from some wave overturning motion (i.e. "rolling motion"), somehow comparable with flow features seen in spilling and plunging breaking waves (CIPRIANO and BLANCHARD 1981, LONGUET-HIGGINS 1982, DEANE 1997, DEANE and STOKES 2002, LUBIN and GLOCKNER 2015). A key difference between breaking waves and breaking bores is the net mass flux during a breaking bore propagation, with a very sudden change in

mass flux direction (STOKER 1957, TRICKER 1965). Herein the air-water flow structures tended to be similar to gas-liquid structures observed in breaking hydraulic jumps (CHANSON 2011b, CHACHEREAU and CHANSON 2011, WANG et al. 2017) and in the upper region of high-speed self-aerated flows (CAIN and WOOD 1981, CHANSON 1997a,b).

In the bore roller, a number of bubbles were entrained below the upper free-surface. Singular aeration took place at the roller toe, in an entrapment motion similar to air entrainment at plunging jets (ERVINE et al. 1980, CUMMINGS and CHANSON 1997, CHANSON et al. 2006). In addition, interfacial exchanges of air were observed through the roller surface, as documented in hydraulic jumps (WANG and CHANSON 2015a, WANG et al. 2017). Visual observations showed rapidly evolving bubble shapes and numbers in response to turbulent shear, bubble-bubble interactions and bubble-free-surface interactions. Figure 6 presents typical examples. In Figure 6A, note the "angular shape" of a number of millimetric bubbles, showing multiple facets.

At the rear of the roller, large aerated vortex filaments, and bathtub-like or tornado-like vortices were seen underwater, as shown in Figure 7. These filaments are similar to those occurring under plunging breaking waves (LUBIN and GLOCKNER 2015) and in turbulent shear flows (HUNT et al. 1988). (For completeness, long aerated vortex filaments were also observed during the rapid gate closure herein. The gate closure induced some water pile-up against the gate and overturning, in a manner similar to a plunging breaking waves, before the bore roller detached from the gate and propagated upstream as detailed by SUN et al. (2016).). The filament lengths ranged typically from about 10 mm to over 50 mm, with millimetric bubbles often between 1 mm and 5 mm sizes (Fig. 7). While the underwater filament were observed at the rear of the roller, where the void fraction was very low, their extremities were often not distinguishable because of the chaotic motion of the highly aerated flow, and could be obscured by bubble clouds and air-water structures. In the present study, however, it was not clear what were the dominant mechanisms responsible for the filament generation and evolution.

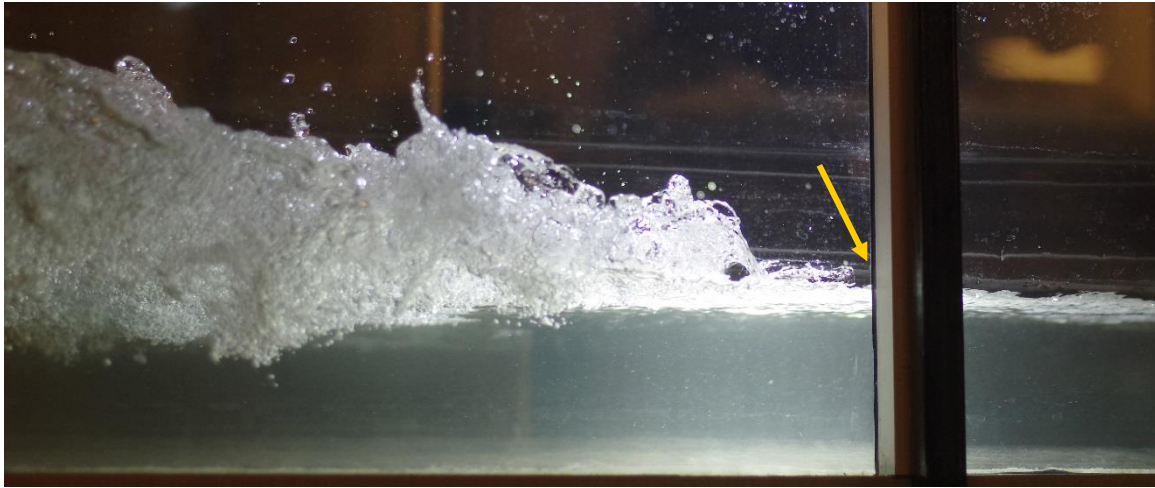
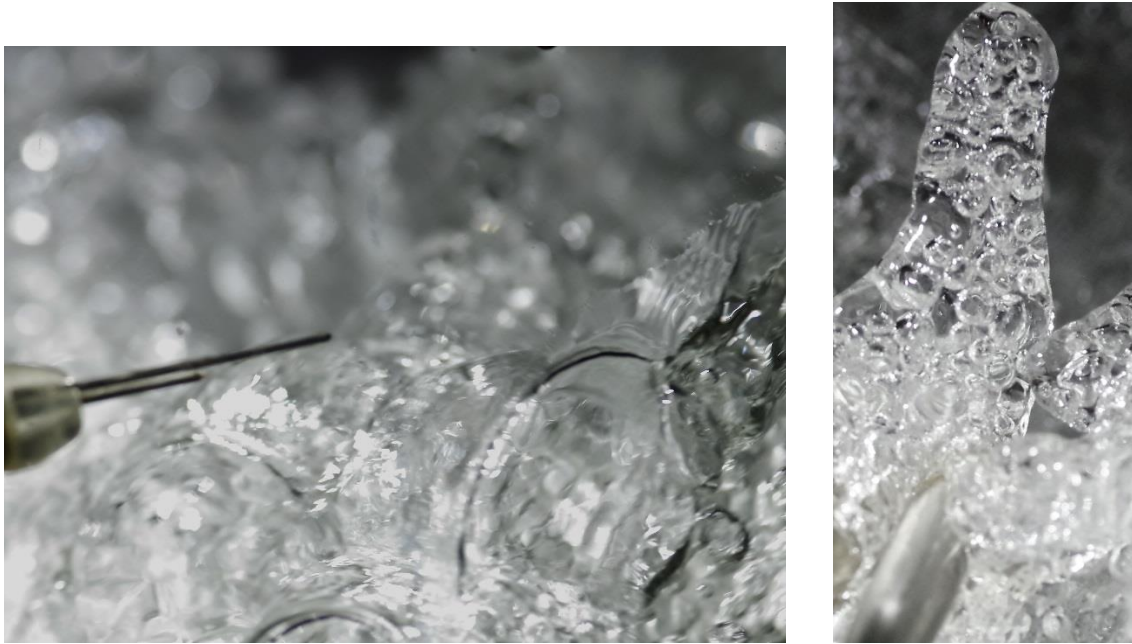


Fig. 4 - Side view of propagating breaking bore (shutter speed: 1/2,000 s) - Flow conditions: $Fr_1 = 2.18$, $d_1 = 0.097$ m, $U = 0.64$ m/s, bore propagation from left to right - Arrow points to onset of droplet ejection ahead of roller



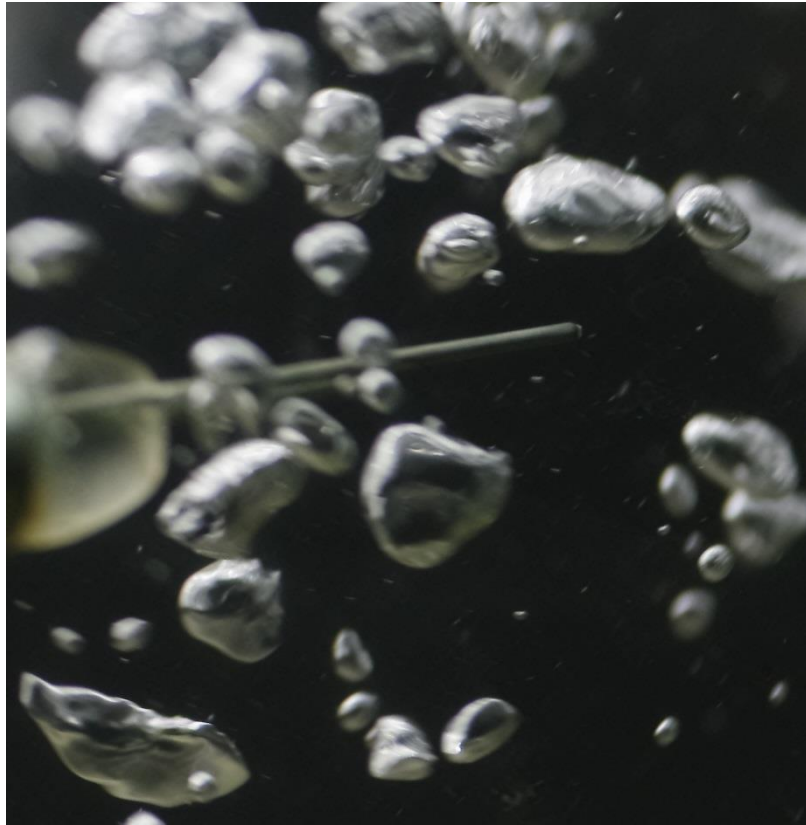
(A) Water droplet ejection ahead of the bore roller, with the dual-tip phase-detection probe leading sensor on the far right of the photograph - Shutter speed: 1/8,000 s, bore propagation direction from right to left, probe located next to right sidewall - Photograph taken about 0.24 s before the roller first impacted the probe leading sensor - The string of ejected droplets was nearly 120 mm long



(B, Left) Foam structure at the leading edge of the breaking bore roller - Shutter speed: 1/2,000 s, bore propagation direction from top right to bottom left - The largest bubble was nearly 10 mm on the right

(C, Right) Phase-detection probe piercing the breaking bore roller free-surface and air-water flow structure above - Shutter speed: 1/8,000 s, bore propagation direction from background to foreground

Fig. 5 - Air-water flow structure observations in a breaking bore - Flow conditions: $Fr_1 = 2.18$, $d_1 = 0.097$ m, $U = 0.64$ m/s - For scale, the dual-tip phase-detection probe leading sensor was about 18 mm long, with 0.8 m outer diameter, while the probe support tube had a 8 mm diameter

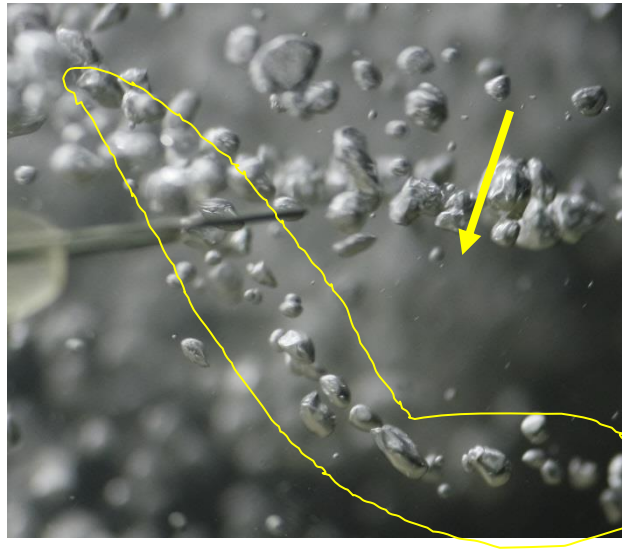


(A) Air bubbles in the roller, next to right sidewall - The photograph was taken about 0.24 s after the roller first impacted the probe leading sensor, located at $z = 0.110$ m ($z/d_1 = 1.134$)

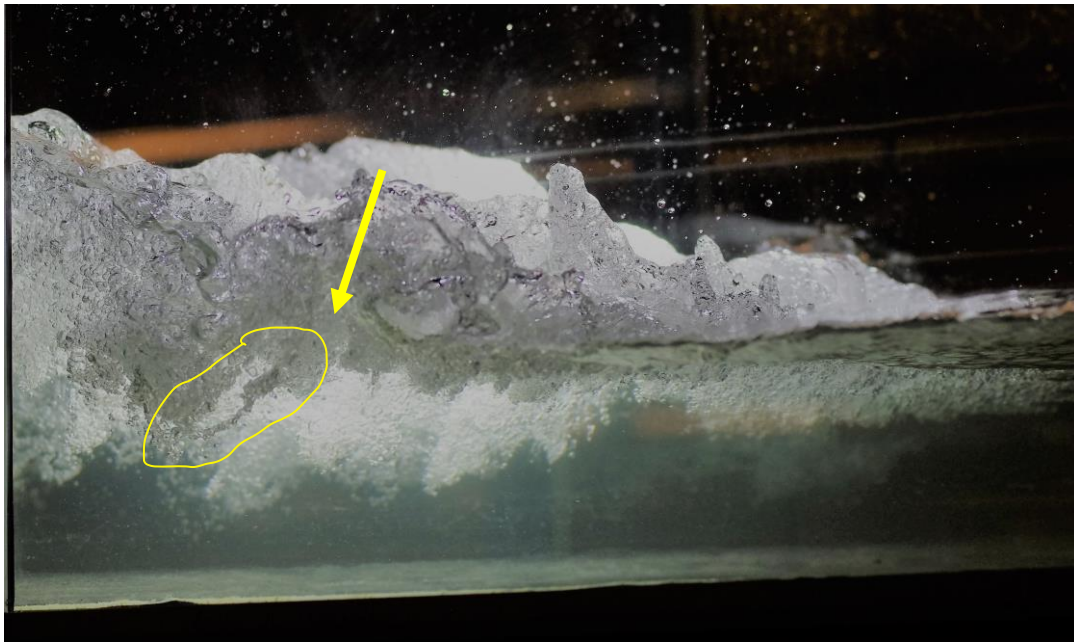


(B) Interactions between dual-tip phase-detection probe sensors and bubbles in the roller, next to right sidewall - in the bubbly flow region of the roller, about 0.84 s after the roller first impacted the probe leading sensor, located at $z = 0.175$ m ($z/d_1 = 1.804$)

Fig. 6 - Bubbly flow structure in a breaking bore - Flow conditions: $Fr_1 = 2.18$, $d_1 = 0.097$ m, $U = 0.64$ m/s - Shutter speed: $1/8,000$ s, bore propagation direction from right to left - For scale, the dual-tip phase-detection probe leading sensor was about 18 mm long, with 0.8 m outer diameter, while the probe support tube had a 8 mm diameter



(A) Photographs taken about 0.60 s after the roller first impacted the probe leading sensor, located at $z = 0.110$ m ($z/d_1 = 1.134$), bore propagation from right to left, shutter speed: $1/8,000$ s, For scale, the dual-tip phase-detection probe leading sensor was about 18 mm long, with 0.8 m outer diameter, while the probe support tube had a 8 mm diameter



(B) Side views of breaking bore roller propagating from left to right, shutter speed: $1/2,000$ s

Fig. 7 - Air-water vortex filament observations in the rear of breaking bore roller (arrow) - Flow conditions: $Fr_1 = 2.18$, $d_1 = 0.097$ m, $U = 0.64$ m/s

3.2 Liquid fraction

The phase-detection probe array detected simultaneously the instantaneous void fraction at several locations (y, z) at the sampling location $x = 8.5$ m. The basic probe output was the

instantaneous void fraction c , defined as $c = 1$ in air and $c = 0$ in water. In practice, an alternative is to consider the instantaneous liquid fraction $(1-c)$, with $(1-c) = 1$ in water and $(1-c) = 0$ in air. (The liquid fraction corresponds to the colour function in LES-VOF CFD modelling (LUBIN et al. 2010, LUBIN and GLOCKNER 2015)). Considering a probe sensor located at $z/d_1 > 1$, the sensor would be initially located in air and the instantaneous liquid fraction would be zero prior to the bore passage. During the bore passage, the sensor would pierce air-to-water interfaces, water-to air- interfaces, water drops and bubbly structures, until the liquid fraction would become unity, as long as the sensor elevation z was below the conjugate water elevation. Herein the time origin was selected as the first detection of an air-to-water interface by the leading sensor of the reference probe, location at $z_{\text{ref}}/d_1 = 1.082$ (i.e. $z_{\text{ref}} = 0.105$ m). The relative arrival time of the first air-to-water interface would depend upon the sensor elevation, with increasing delay with increasing elevation above the initial water surface.

The experimental measurements were repeated at 33 different vertical elevations. Namely, one run was performed at each elevation z . Typical instantaneous liquid fraction $(1-c)$ data in the bore roller are presented Figure 8. Full data sets are reported in LENG and CHANSON (2018). Figure 8 shows the two-dimensional distributions of liquid fraction, in the form of a contour plot. The experimental measurements indicated a relatively short and thin air-water flow region. While the air-water flow region was about 0.6 m long (i.e. $L_{\text{air}}/d_1 \approx 6.2$), the aerated interfacial zone was 0.05 m to 0.15 m thick only. That is, the entrained air did not penetrate deep into the roller region, although a few individual bubbles were seen advected behind and below the breaking bore roller, as illustrated in Figure 7. For completeness, the results were very close for all four probe sensors (Probes 1 & 2).

Overall the data showed that the air-water bubbly flow region of the roller was relatively small (Fig. 8). The findings were consistent with air-water flow measurements in stationary hydraulic jumps at low Froude numbers (MURZYN et al. 2005, CHACHEREAU and CHANSON 2011). A characteristic feature of breaking bore roller was the large amount of spray and droplets above and in front of the roller. The spray region interacted with the atmosphere and induced some short-lived air flux above the water surface. A related effect of air bubble entrainment was the relatively loud noises generated by the bore roller. The sound of the breaking bore was relatively low-pitch and had a characteristic frequency close to the collective oscillations of bubble clouds, linked to a transverse dimension of the bore roller (CHANSON 2016b).

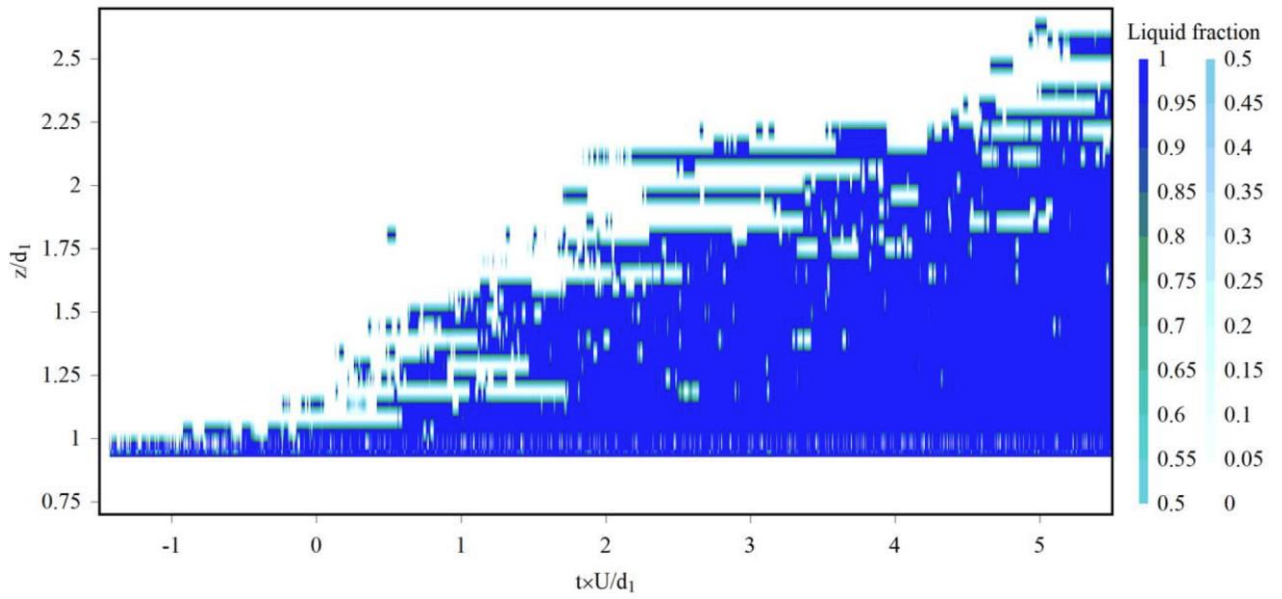


Fig. 8 - Dimensionless contour plot of instantaneous liquid fraction in a breaking bore - Probe 2, left sensor: $x = 8.50$ m, $y = 0.231$ m, Flow conditions: $Fr_1 = 2.18$, $d_1 = 0.097$ m, $U = 0.64$ m/s - Colour scale shows the liquid fraction between 0 and 1

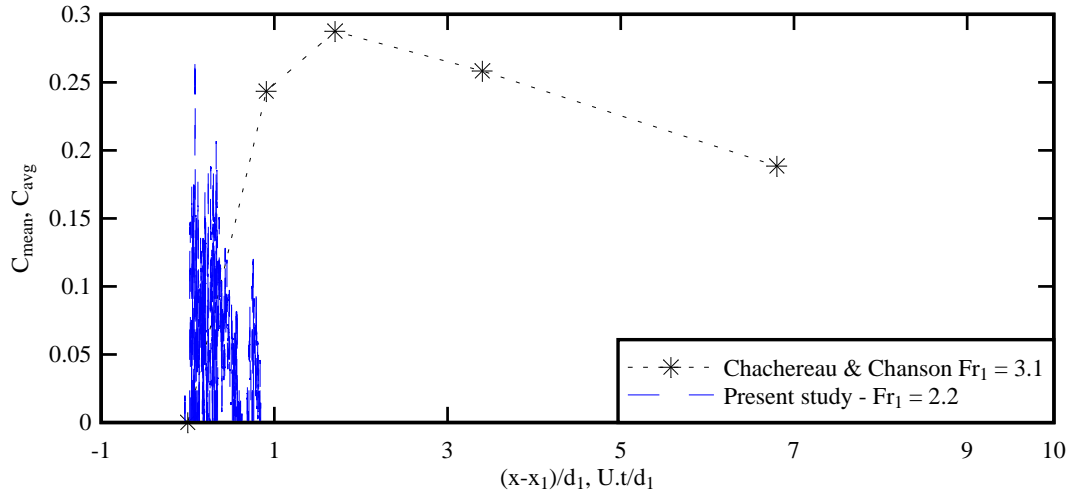
3.3 Void fraction

Based upon the instantaneous vertical distributions of void fraction c , a depth-averaged mean void fraction C_{avg} was calculated as:

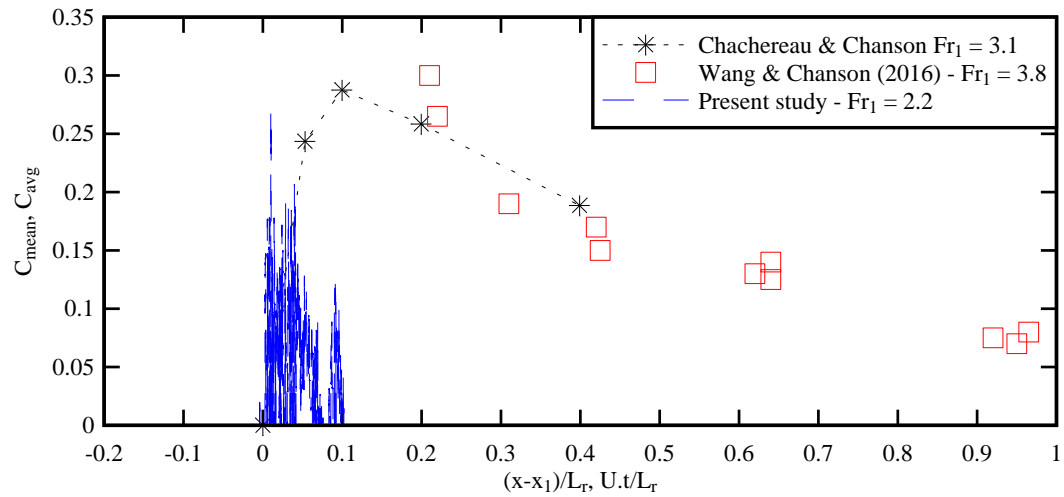
$$C_{avg} = \frac{1}{Z_{max}} \int_{z=0}^{z=Z_{max}} c \times dz \quad (1)$$

where z_{max} is the instantaneous highest elevation (¹) where liquid fraction was detected (i.e. $1 - c = 1$). The depth-averaged mean void fraction C_{avg} is comparable to the mean void fraction C_{mean} defined in terms of the 90% void fraction elevation Z_{90} and integrated from zero up to Z_{90} , in self-aerated steady flows and stationary hydraulic jumps (WOOD 1991, CHANSON 1997a). Experimental results are presented in Figure 9, where they are compared with experimental observations in stationary hydraulic jumps with low Froude numbers (CHACHEREAU and CHANSON 2011, WANG 2014, WANG and CHANSON 2016).

¹ out of the 33 sampling elevations.



(A) Depth-averaged mean void fraction as a function of the dimensionless distance $(x-x_1)/d_1$

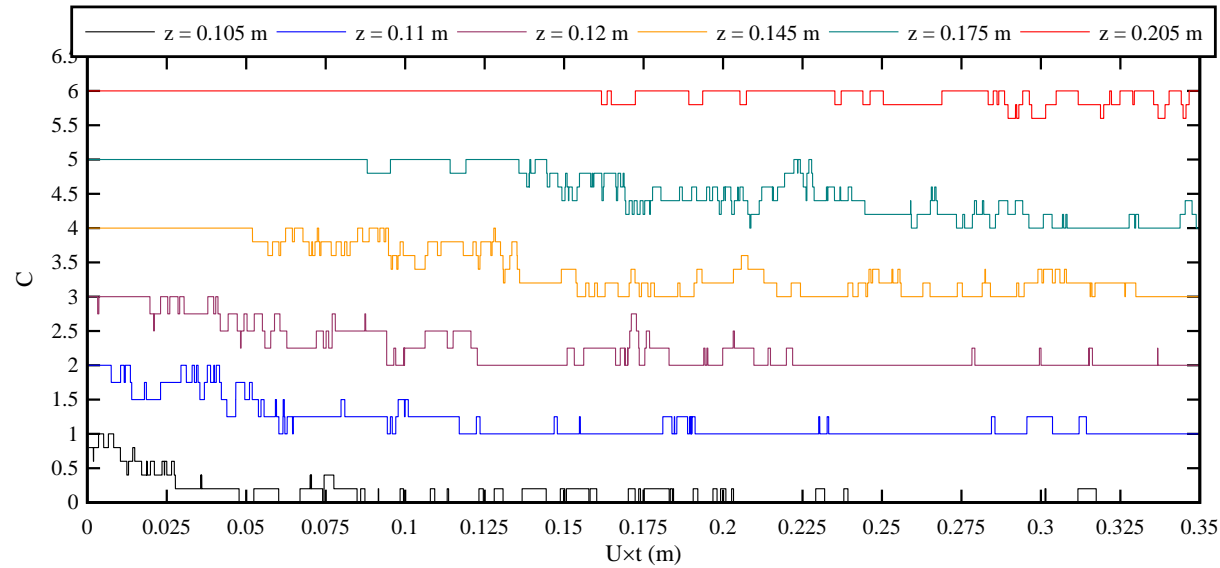


(B) Depth-averaged mean void fraction as a function of the roller location $(x-x_1)/L_r$

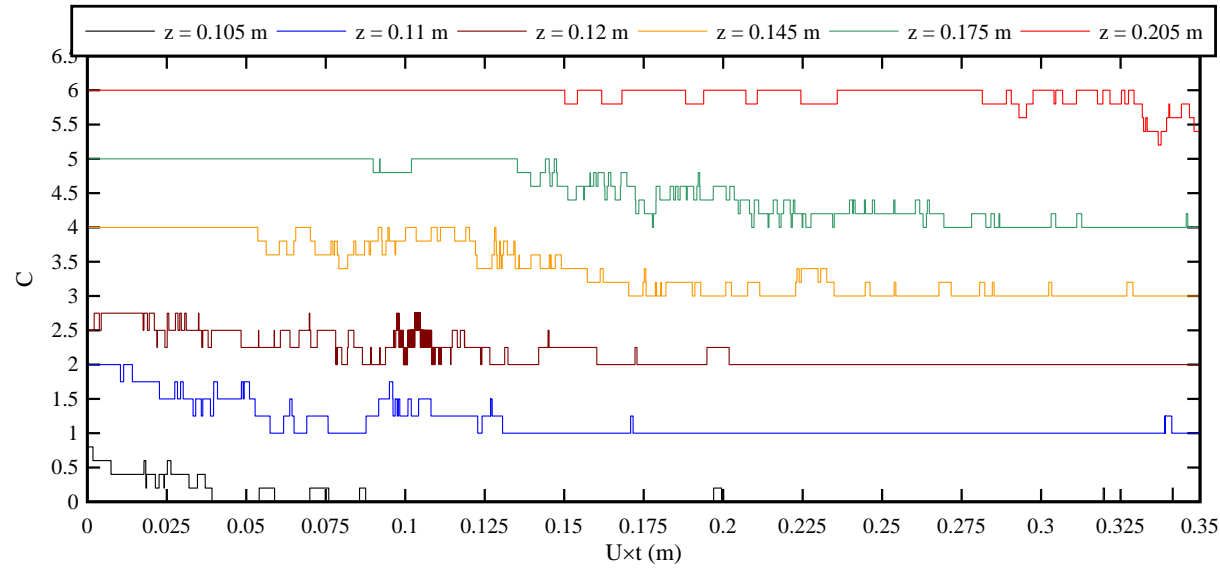
Fig. 9 - Longitudinal distribution of depth-averaged mean void fraction C_{avg} in breaking bore - Data set: Probe 2 right sensor - Comparison with mean void fraction C_{mean} data in stationary hydraulic jumps - x_1 is the longitudinal position of the roller toe (CHACHEREAU and CHANSON 2011, WANG and CHANSON 2016)

A key feature of present observations is the small amount of entrained air and the limited extent of the aerated zone in the roller. This is unlike stationary jumps, although there are key differences in the experimental data collection of void fraction, between present breaking bore experiments and stationary hydraulic jumps. The former constituted of continuous time-series records sampled at 100 kHz, providing a very-high level of details next to the roller toe. The latter were point measurements with long-continuous records delivering precise time-averaged data.

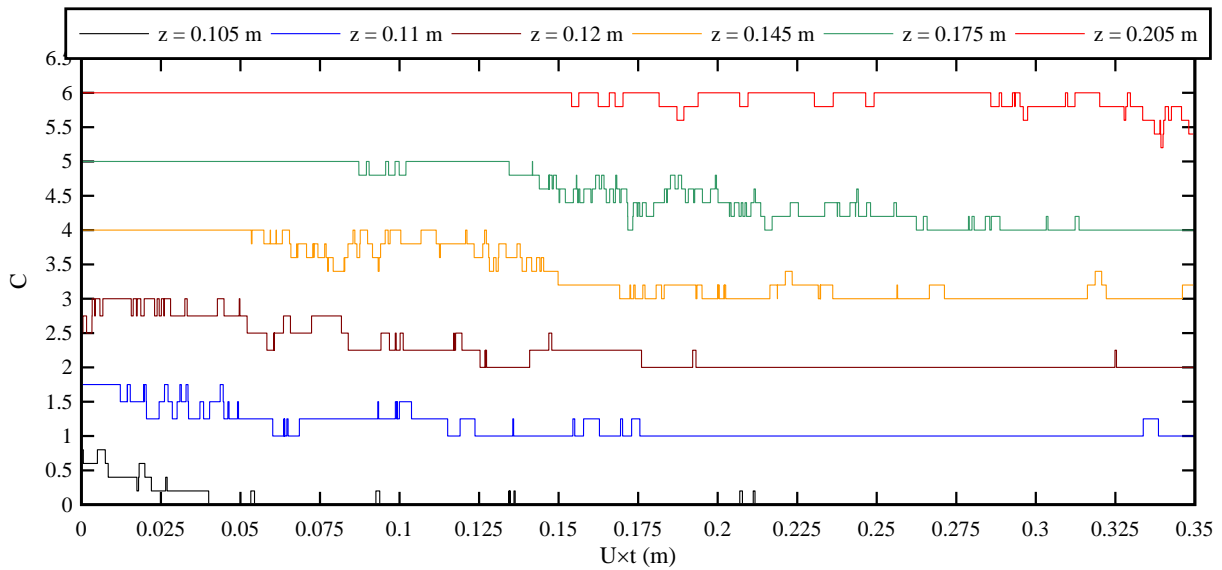
Ensemble-averaged void fraction can be calculated at a certain vertical location by ensemble-averaging the instantaneous void fraction over the number of repeated measurements, in this case, 5 repeats (experiment series 2). The data showed self-similar variations with time at different probe locations (Fig. 10). A gradual delay of the detection of the first air-water interface was observed with increasing vertical elevation, highlighting the free-surface curvature of a breaking roller in the x-z plane. At all elevations, the ensemble-averaged void fraction showed high values close to the roller toe. The region with intense aeration, indicated by a cluster of large void fraction values, was observed roughly 0.05 to 0.1 m downstream of the roller toe.



(A) Probe 1 leading tip



(B) Probe 2 left tip



(C) Probe 2 right tip

Fig. 10 - Ensemble-averaged void fraction measured by an array of dual-tip phase-detection probe at different vertical elevations - Flow conditions: $Q = 0.101 \text{ m}^3/\text{s}$, $Fr_1 = 2.18$, $d_1 = 0.097 \text{ m}$, $U = 0.64 \text{ m/s}$ - Void fraction C offset by +1 for every higher vertical elevation

4. Discussion

4.1 Roller characteristics in breaking bores

A key feature of breaking bores, jumps and spilling breakers is the roller region (LUBIN and CHANSON 2017). The roller is a highly turbulent flow characterised by intense shear and recirculation, associated with air bubble entrainment, splashing, spray and energy dissipation (TRICKER 1965, HOYT and SELLIN 1989). Historically, the roller dimensions were experimentally derived from experimental observations, typically the roller height ($d_2 - d_1$), its length L_r and the air-water flow region length L_{air} (Fig. 11). A review of experimental observations was conducted, including breaking bores, stationary hydraulic jumps, and steady breaker. (For completeness, LUBIN and CHANSON (2017) reported a few additional data.) Basic flow conditions of laboratory experiments and field observations are summarised in Table 2. The comparative data regroup breaking bore observations in laboratory and in the field, hydraulic jump data at low inflow Froude numbers, and steady breaker behind a submerged hydrofoil. In the following paragraphs, the experimental data are presented in two fashions, i.e. using the inflow depth d_1 or roller height ($d_2 - d_1$) as the characteristic length scale.

For a smooth horizontal rectangular channel, the application of the momentum principle to a stationary hydraulic jump and a breaking bore gives the classical Bélanger equation:

$$\frac{d_2}{d_1} = \frac{1}{2} \times \left(\sqrt{1 + 8 \times Fr_1^2} - 1 \right) \quad (2)$$

where $Fr_1 = (V_1 + U)/(g \times d_1)^{1/2}$. After transformation, the momentum principle yields a parabolic relationship between the dimensionless roller height $(d_2 - d_1)/d_1$ and the Froude number defined in terms of the roller height $(V_1 + U)/(g \times (d_2 - d_1))^{1/2}$

$$\left(3 + \frac{d_2 - d_1}{d_1} \right)^2 - 1 = 8 \times \frac{d_2 - d_1}{d_1} \times \left(\frac{V_1 + U}{\sqrt{g \times (d_2 - d_1)}} \right)^2 \quad (3)$$

Equation (3) exhibits a minimum $((V_1 + U)/(g \times (d_2 - d_1))^{1/2})_{\min} = 1.707$ corresponding to a critical roller height $(d_2 - d_1)/d_1 = 1.41$, as illustrated in Figure 12 (Right). Experimental observations of conjugate depths and roller heights are presented as functions of the Froude number in Figure 12, for laboratory experiments of breaking bores and stationary hydraulic jumps, and field observations of tidal bores. The physical data are compared to the momentum principle applied to a smooth rectangular channel (Eq. (2) & (3)). The ratio of conjugate depth data showed a close agreement between all data and the Bélanger equation (Eq. (2)) (Fig. 12 Left). In contrast the dimensionless roller height data presented some scatter about the theoretical results, particularly close to the minimum in Froude number (Fig. 12 Right).

A review of roller length observations is presented in Figure 13 and 14. In Figures 13 (Left) and 14 (Left), the roller length L_r and air-water region length L_{air} are shown in a traditional way, with L/d_1 as a function of the Froude number Fr_1 , the initial flow depth d_1 being the characteristic length scale. In contrast, Figures 13 (Right) and 14 (Right) present the dimensionless data, using the roller height $(d_2 - d_1)$ as characteristic length scale. On all graphs, WANG's (2014) correlation for the hydraulic jump roller length is plotted as a solid line. Overall the present findings showed comparable roller dimensions between breaking bores, stationary hydraulic jumps and steady breaker for comparable dimensionless flow conditions.

LENG, X., and CHANSON, H. (2019). "Air-Water Interaction and Characteristics in Breaking Bores." *International Journal of Multiphase Flow*, Vol. 120, Paper 103101, 17 pages (DOI: 10.1016/j.ijmultiphaseflow.2019.103101) (ISSN 0301-9322).

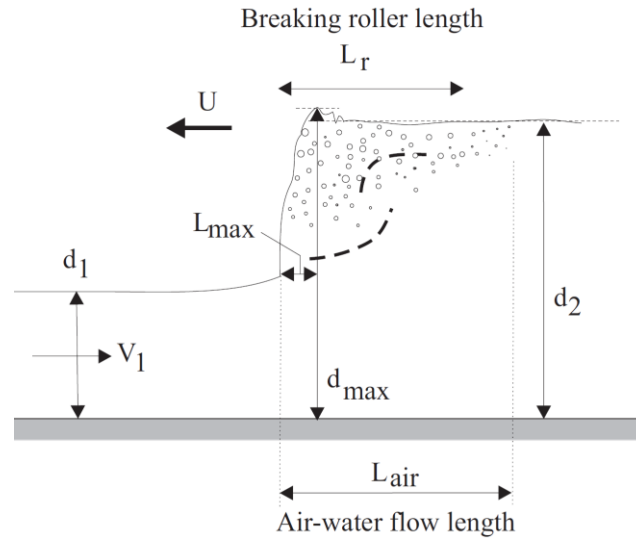


Fig. 11 - Definition sketch of a breaking bore and its roller

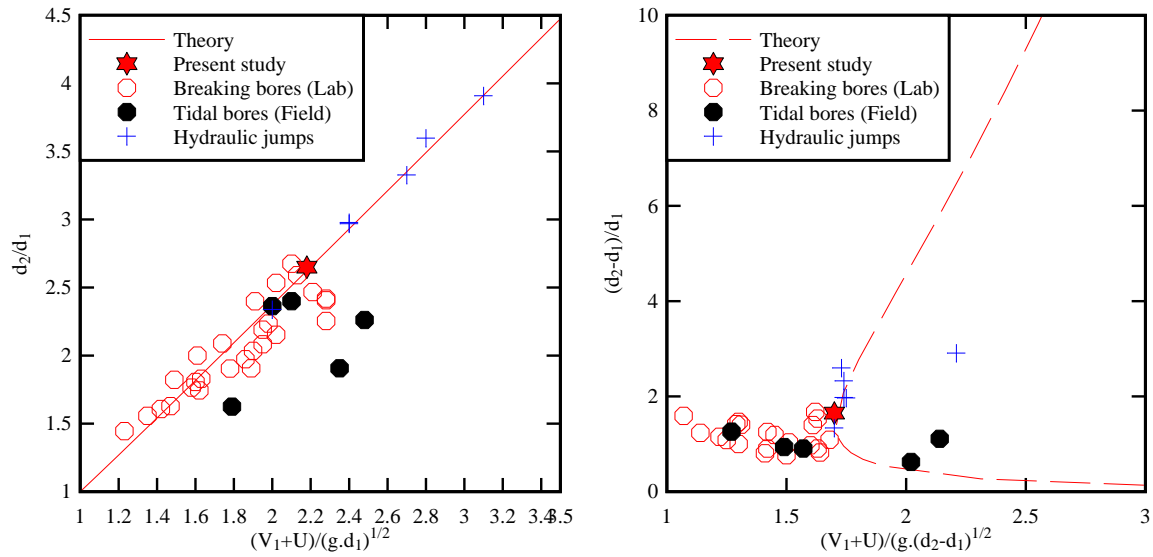
Table 2 - Experimental observations in breaking bores, roller and jumps

Ref.	S_o	B_1 (m)	V_1 (m/s)	d_1 (m/s)	U (m/s)	Fr_1	Configuration
Present study	0.0075	0.70	1.49	0.097	0.64	2.18	Travelling bore.
CHANSON & TOI (2015)	0.025	0.50	0.97	0.05	0.26-0.53	1.7-2.1	Travelling bore.
LENG & CHANSON (2015a)	0	0.70	0.83	0.146	0.95	1.49	Travelling bore.
LENG & CHANSON (2017b)	0-0.0075	0.70	0.82-1.46	0.086-0.175	--	1.23-2.2	Travelling bore.
SIMPSON et al. (2004)	--	68.3	0.15	0.72	4.1	1.79	Dee River tidal bore on 6 Sept. 2003
MOUAZE et al. (2010)	--	33-35	0.59-0.86	0.325-0.375	1.96-2	2.35-2.48	Sélune River tidal bore on 24 Sept. 2010
Qiantang River tidal bore (¹)	--	3500	--	1	3.65	2.1	Daquekou (northern channel) on 6 Sept. 2013
	--	2500	1	1.6-2.2	4.35-7.85	1.5-2	Yanguan between 12 & 23 Oct. 2014.
CHACHEREAU & CHANSON (2011)	0	0.50	2.48	0.044	0	3.1	Stationary hydraulic jump
MURZYN et al. (2005)	0	0.30	1.50	0.059	0	2.0	Stationary hydraulic jump
COAKLEY et al. (2001)	0	6.7	1.01	--	2.42	--	Steady breaker behind a towed submerged NACA0012 foil

Notes: B_1 : initial free-surface width; d_1 : inflow depth; d_2 : conjugate depth; L_{air} : air-water flow region length; L_r : roller length; S_o : bed slope; U : bore celerity for an observer standing on bank;

LENG, X., and CHANSON, H. (2019). "Air-Water Interaction and Characteristics in Breaking Bores." *International Journal of Multiphase Flow*, Vol. 120, Paper 103101, 17 pages (DOI: 10.1016/j.ijmultiphaseflow.2019.103101) (ISSN 0301-9322).

V_1 : inflow velocity; $(^1)$: references LENG and CHANSON (2015c), CHANSON (2016b) and Present study.



(A) Relationship between the conjugate depth ratio d_2/d_1 and Froude number $(V_1+U)/(g \times d_1)^{1/2}$ - Comparison between experimental data and the Bélanger equation (Eq. (2)).

(B, Right) Dimensionless relationship between the roller height $(d_2-d_1)/d_1$ and Froude number defined in terms of the roller height $(V_1+U)/(g \times (d_2-d_1))^{1/2}$ - Comparison between experimental data and momentum considerations for a smooth horizontal rectangular channel (Eq. (3))

Fig. 12 - Dimensionless relationship between the conjugate depth, roller height and Froude number

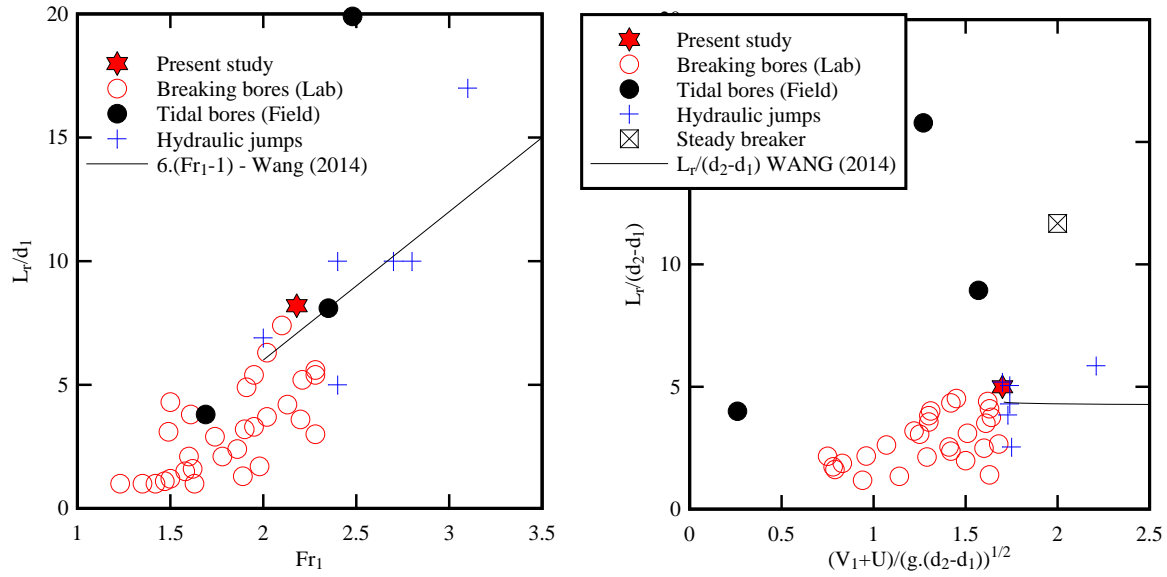


Fig. 13 - Dimensionless roller length in breaking bores (laboratory and field data) and stationary hydraulic jumps at low inflow Froude numbers - Comparison with WANG's (2014) correlation

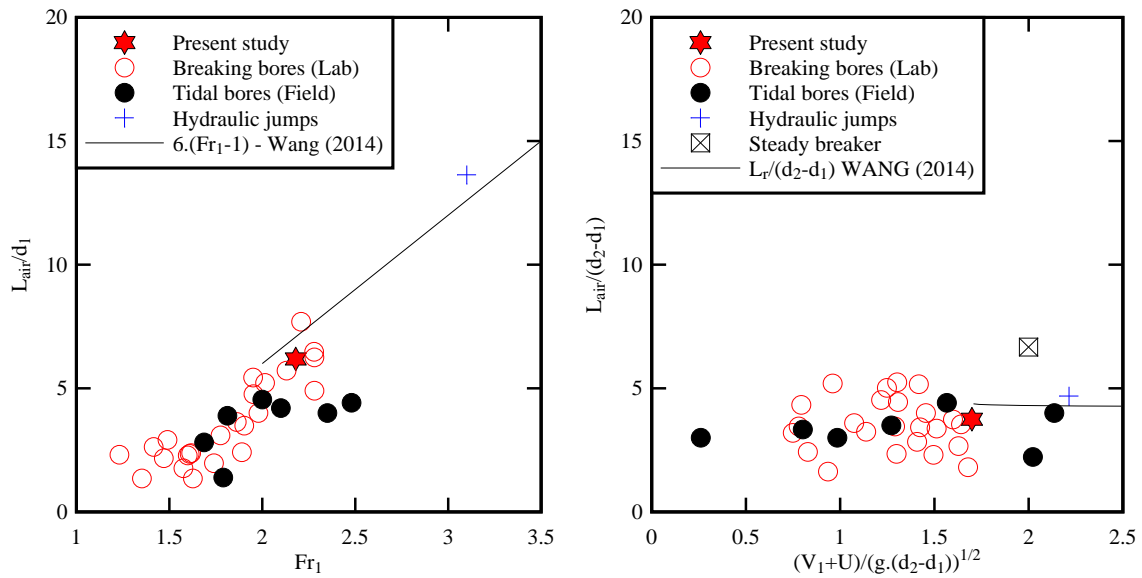


Fig. 14 - Dimensionless air-water flow length in breaking bores (laboratory and field data), stationary hydraulic jumps at low inflow Froude numbers, and steady breaker behind a submerged hydrofoil - Comparison with WANG's (2014) correlation for the roller length

4.2 Bubble characteristics

The bubble chord times were measured at several elevations (experiments series 1 and 3). Typical bubble chord distribution data are shown in Figure 15. In Figure 15A, each figure

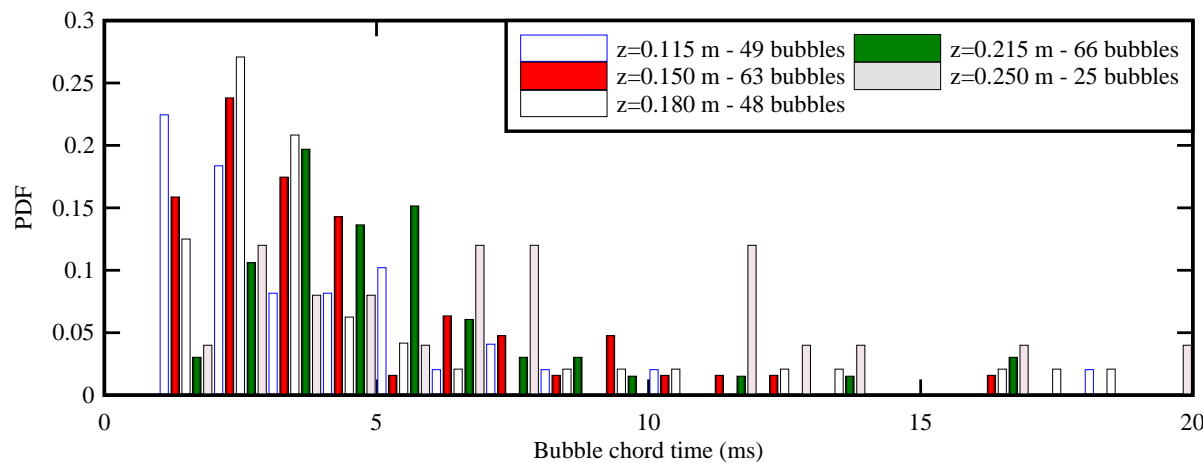
shows the normalized probability distribution function of bubble chord time t_{ch} where the histogram columns represent the probability of chord time in 1-ms intervals: e.g., the probability of chord length from 1.0 to 2.0 ms is represented by the column labelled 2.0. Figure 15B presents typical normalized probability distribution functions of bubble chord length ch where the histogram columns represent the probability of chord time in 1-mm intervals: e.g., the probability of chord length from 2.0 to 3.0 mm is represented by the column labelled 3.0. For all elevations and investigated bore conditions, the data demonstrated a broad spectrum of pseudo-bubble chord sizes: i.e., from less than 0.1 mm to more than 50 mm. The bubble chord length distributions were skewed with a preponderance of small bubble chord sizes relative to the mean (Fig. 15) and they tended to follow a log-normal distribution, albeit the data sets were relatively small. The probability of bubble chord length was the largest for pseudo-bubble chord sizes between 1 and 3 mm, although the median pseudo-chord size was about 1 to 6 mm. The trends were emphasized by positive skewness and large kurtosis. Overall, the number of detected bubbles was small at all elevations (Fig. 16A), while large bubble chords could correspond to overturning wave motion rather than 'true' bubbles. The small number of detected bubbles was consistent with the void fraction data (Section 3). Although the finding might appear to contradict photographic observations, a phase-detection probe sensor recorded point-like measurements (the sensor size was 0.25 mm), when photographs caught bubbles within the depth of field of the lens. That is, 20 mm to more than 200 mm depending upon the lens aperture and camera settings. Vertical distributions of first quartile, second quartile (i.e. median) and third quartile of bubble chord times and lengths are presented in Figure 16.

The bubble chord data showed consistently an increasing bubble chord time and length with increasing vertical elevations z/d_1 , as previously reported by LENG and CHANSON (2015a) albeit for a much smaller data set (Fig. 16). The largest number of bubbles were detected between $z/d_1 = 1.2$ and 2.2 (Fig. 16A). Such a range of vertical elevations corresponded approximately to the bulk of the aerated roller region. In Figure 16A, note the good agreement between single-run data (Series 1) and ensemble averaged data (Series 3).

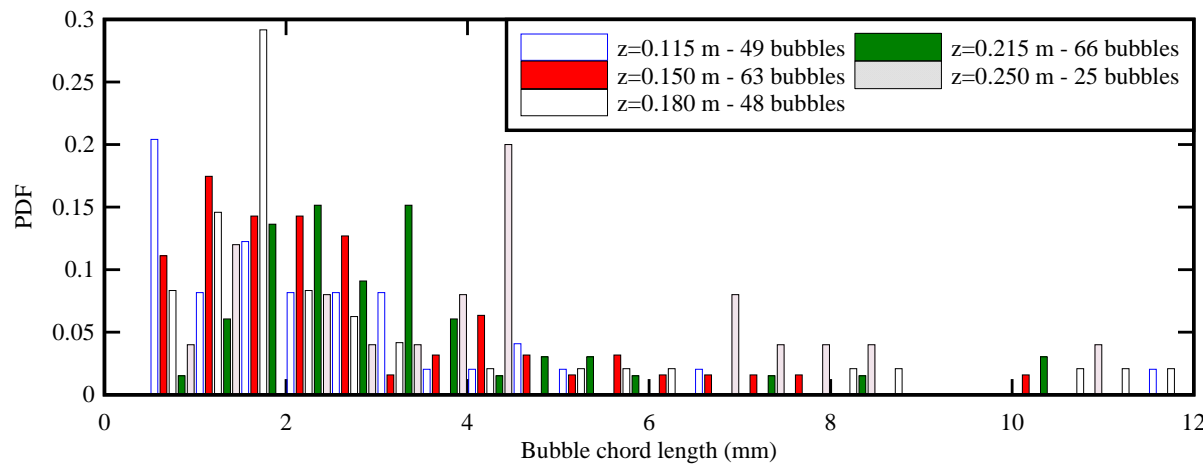
The present results were compared to previous studies in breaking bores (LENG and CHANSON 2015a) and stationary hydraulic jumps (CHACHEREAU and CHANSON 2011) (Table 3). In all studies, a large majority of detected bubbles had a chord time of 5-8 ms or less, with a mode about 1-2 ms. The present data showed a comparable a range of bubble chord time, with increasing bubble chord with increasing elevation in the roller. At the highest elevations, the probe sensor interacted with the upper free-surface and water drops, and both surface waves

and surface roughness influenced significantly the chord time distributions, with an increased percentage of large chords (TOOMBES and CHANSON 2007).

High-shutter speed photographs showed a substantial number of bubbles with millimetric sizes: i.e., between 1 to 5 mm (Section 3). Photographic observations were comparable to previous photographic observations and acoustic bubble size distributions in breaking bores (Table 3). Note that, in CHANSON (2010), bubble radii were derived from the transient underwater acoustic signature of the bore. Although bubble sizes are not strictly comparable to bubble radii, present observations were of the same order of magnitude as the acoustic bubble radii of CHANSON (2010).

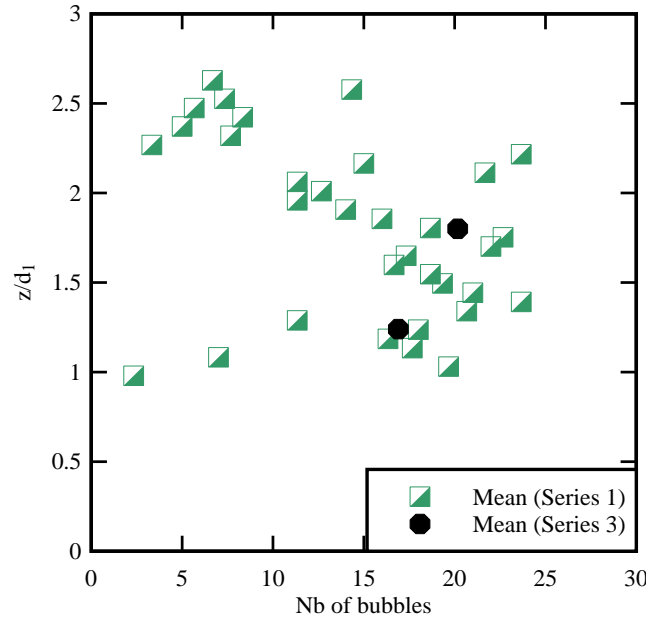


(A) Bubble chord time data

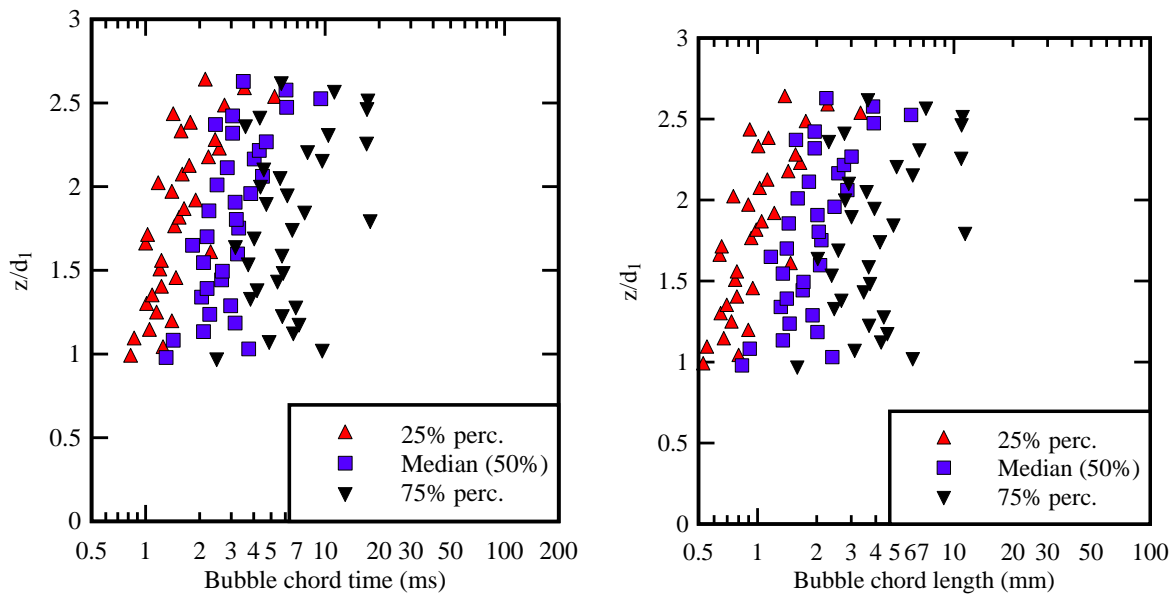


(B) Pseudo-bubble chord length data

Fig. 15 - Probability distribution functions of bubble chord in a breaking roller - Experiments Series 1, data ensemble: Probe 1 leading sensor, Probe 2 left sensor and Probe 2 right sensor



(A) Mean number of bubbles detected per probe sensor per run (Series 1 and 3)



(B, Left) Statistical properties (percentiles) of bubble chord times (ms) (Series 1)

(C, Right) Statistical properties (percentiles) of bubble chord lengths (mm) (Series 1)

Fig. 16 - Vertical distributions of bubble size properties in a breaking bore roller - Experiments Series 1, data ensemble: Probe 1 leading sensor, Probe 2 left sensor and Probe 2 right sensor; Experiments Series 3, data ensemble: Probe 2 left sensor

LENG, X., and CHANSON, H. (2019). "Air-Water Interaction and Characteristics in Breaking Bores." *International Journal of Multiphase Flow*, Vol. 120, Paper 103101, 17 pages (DOI: 10.1016/j.ijmultiphaseflow.2019.103101) (ISSN 0301-9322).

Table 3 - Experimental investigations of bubble/drop particle sizes in breaking bores and hydraulic jumps

Reference	S_o	B_1 (m)	Q (m ³ /s)	d_1 (m)	V_1 (m/s)	\bar{U} (m/s)	Fr_1	Instrumentation
Breaking bores								
Present study	0.0075	0.70	0.101	0.097	1.49	0.64	2.18	Phase-detection probe array, dSLR photography (24 Mpx) at x = 8.5 m
CHANSON (2010)	0	0.50	0.026 0.043 0.056	0.100 0.138 0.116	0.52 0.63 0.97	0.82 0.95 0.83	1.36 1.36 1.68	Hydrophone Dolphin Ear
LENG & CHANSON (2015a)	0	0.70	0.085 0.085 0.085 0.085	0.160 0.146 0.146 0.160	0.76 0.83 0.83 0.76	0.99 0.95 0.95 0.97	1.40 1.49 1.49 1.38	Video (25 fps) at x = 6.6 m Video (50 fps) at x = 6.6 m Phase-detection probe at x = 7.1 m Phase-detection probe at x = 7.1 m
			0.085	0.165	0.74	0.90	1.33	Video (120, 240, 480 fps) at x = 9.2 m
Hydraulic jumps								
CHACHEREAU & CHANSON (2011)	0	0.50	0.0446	0.044	2.01	0	3.1	Phase-detection probe, dSLR photography (12 Mpx).

Notes: B_1 : initial free-surface width; d_1 : initial water depth at sampling point; Fr_1 : bore Froude number: $Fr_1 = (\bar{U} + V_1)/(g \times d_1)^{1/2}$; S_o : bed slope; \bar{U} : cross-sectional time-averaged bore celerity recorded at sampling point; V_1 : initial flow velocity recorded at sampling point; x: longitudinal distance from upstream end of glass sidewalled channel.

4.3 Bubble clustering

In a breaking bore roller, a study of particle clustering is relevant to infer whether the formation frequency responds to some particular frequencies of the flow. The clustering level may provide a quantitative measure of the magnitude of bubble-turbulence interactions, including coupling and modulation, and associated turbulent dissipation. In the bubbly region, clustering is linked to the effects of inter-particle turbulent interactions as well as the effects of inertial forces leading to bubble trapping, hence clustering, in large-scale turbulent eddies. When a bubble is trapped in a vortical structure, the centrifugal pressure gradient moves the bubble inside the coherent structure core where bubble-bubble interactions may further take place (TOOBY et al. 1977, SENE et al. 1994). Bubble clustering characteristics may further be

compared to other related air-water flows (CHANSON et al. 2006, CHANSON 2007, SUN and CHANSON 2013, WANG et al. 2015).

A cluster is defined as a group of two or more bubbles, with a distinct separation from other bubbles (Fig. 17). Herein the streamwise distribution of bubbles was analysed. Based upon the analysis of the water chord between two successive bubbles, the bubbles may be considered a group/platoon/cluster when the two neighbouring bubbles are closer than a characteristic length or time scale. In the present study, the characteristic length/time scale was related to the bubble chord size/time itself, since bubbles within some distance may be influenced by the leading particle (CHANSON et al. 2006). Considering a group of two bubbles, the trailing particle may be adversely affected in the near-wake of the lead bubble, since the wake length is about 0.5 to 2 times the particle size for spheroids at large-particle Reynolds numbers (CLIFT et al. 1978). Such a criterion, based upon the near-wake concept, is considered to be particularly relevant to complex air-water flows because it relies on a comparison between the local characteristic flow scales, namely the water chord and the air chord of the preceding bubble (GUALTIERI and CHANSON 2010).

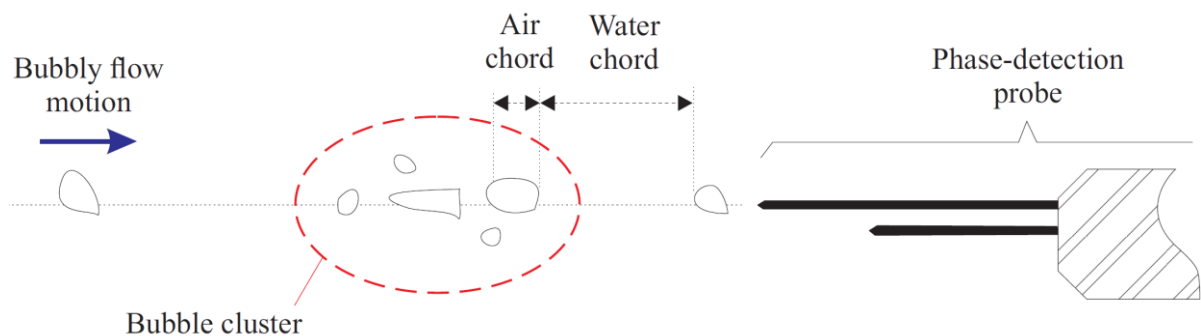


Fig. 17 - Sketch of air bubble cluster and individual air bubbles impacting the phase-detection probe

Two successive bubbles were defined herein as a cluster when the trailing bubble was separated from the lead particle by a water chord smaller than one lead bubble chord, following earlier studies (CHANSON et al. 2006, GUALTIERI and CHANSON 2010). Importantly the present analysis was conducted along a streamline and did not consider bubbles travelling side by side, as being part of a cluster. For discussions on two-dimensional clustering, see SUN and CHANSON (2013) and WANG et al. (2015). The cluster analysis was performed in terms of the air-water chord time data set. For the experimental Series 1, the chord time data ensemble included the Probe 1 leading sensor, the Probe 2 left sensor and the Probe 2 right sensor. At

each vertical elevation, the bubble cluster statistical results were ensemble-averaged. The detailed data are presented in Figure 18 in terms of the percentage of bubbles in clusters and number of bubbles per cluster.

Overall the results showed that more than 50% of all bubbles travelled as part of a cluster structure. The mean cluster size was about 2.5-3.5 particles in average, although large bubble clusters with up to 7-8 bubbles were detected. The results presented no trend in terms of vertical elevation within the roller. Interestingly the present findings were close to clustering properties in stationary hydraulic jumps with low Froude numbers (CHACHEREAU and CHANSON 2011, WANG 2014), despite the drastically lesser number of entrained bubbles in the present breaking bore investigation.

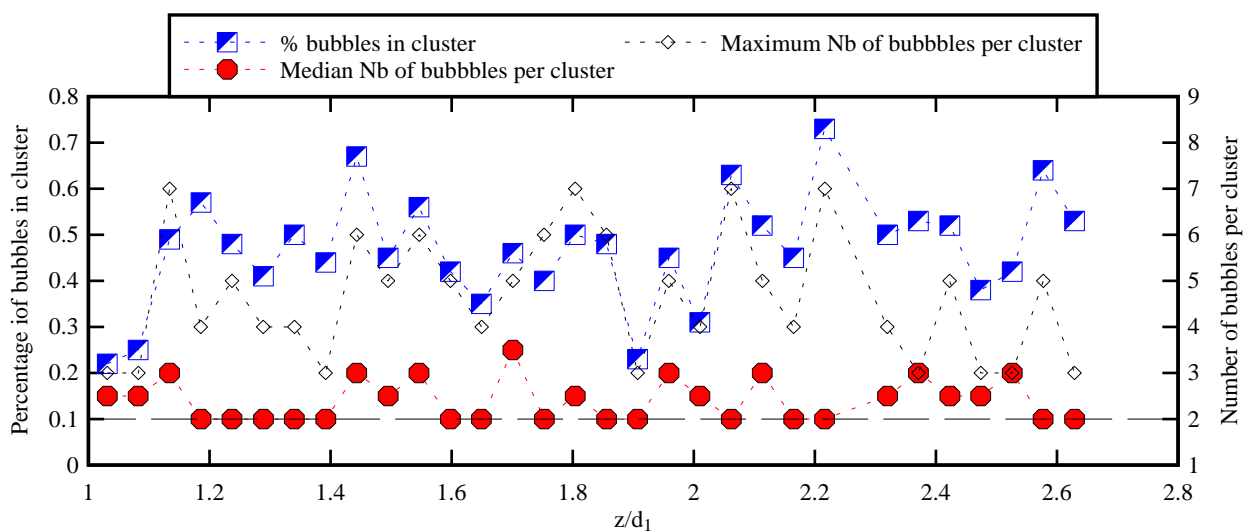


Fig. 18 - Vertical distributions of percentage of bubbles in clusters, median number of bubbles per cluster and maximum number of bubbles per cluster in a breaking bore roller

5. Conclusion

New experiments were conducted in relatively large physical facility with a focus on the microscopic air-water flow properties in the breaking bore roller. Measurements using an array of phase-detection probes, coupled with a series of acoustic displacement meters, were performed to study the unsteady air entrainment process in breaking bores. Detailed visual examination was undertaken using high-resolution high-shutter-speed photography. A range of air-water properties were investigated in detail, including liquid fractions, void fractions, aerated roller characteristics and bubble clustering.

The study found that air entrainment takes place in the form of air entrapment at the roller toe, air-water exchange across the roller 'free-surface', spray and splashing with dynamic water drop ejection and reattachment, roll up and roll down of water 'tongues' engulfing air pockets. While the breaking roller was aerated, the amount of entrained air was quantitatively small for $Fr_1 = 2.2$. All experimental measurements indicated a relatively short and thin air-water flow region. The number of air bubbles within the roller was limited, with between 5 to 20 bubbles per phase-detection probe sensor detected at each vertical elevation, within $1.2 < z/d_1 < 2.5$. The entrained air bubble chord lengths spanned over several orders of magnitude, with many bubbles between 0.7 mm to 5 mm, and an increasing chord size with increasing vertical elevation within the roller. A large proportion of clustered bubbles were observed and the clustering characteristics were similar to those in stationary hydraulic jumps. The roller length and air-water flow region length were closely linked to the Froude number Fr_1 like in stationary hydraulic jumps, and the roller height was linked to the Froude number and the relationship followed closely theoretical relationship derived based upon continuity and momentum principles.

Overall, the study delivers the first systematic physical data to detail the air-water characteristics in a travelling breaking bore or breaking jump. The results could serve as a validation frame for computational fluid dynamics (CFD) modelling, as the modelling of air-water interactions in breaking rollers of hydraulic jumps and tidal bores remain a huge challenge for numerical modeller.

6. Acknowledgement

The authors thank Dr Hubert BRANGER (IRPHE, University of Marseille, France) and Dr Jorge LEANDRO (Technical University of Munich, Germany) for their valuable comments. They acknowledge the helpful inputs of Professor Pierre LUBIN (University of Bordeaux, France) and Dr Hang WANG (Sichuan University, China), as well as discussions with Dr Gangfu ZHANG (WSP, Australia) and Dr Matthias KRAMER (The University of New South Wales Canberra, Australia). The first author is grateful for the supervisory contributions of Professor Pierre LUBIN (University of Bordeaux, France) and Dr Hang WANG (Sichuan University, China). The technical assistance of Jason VAN DER GEVEL and Stewart MATTHEWS (The University of Queensland, Australia) is greatly appreciated.

LENG, X., and CHANSON, H. (2019). "Air-Water Interaction and Characteristics in Breaking Bores." *International Journal of Multiphase Flow*, Vol. 120, Paper 103101, 17 pages (DOI: 10.1016/j.ijmultiphaseflow.2019.103101) (ISSN 0301-9322).



References

- BREDMOSE, H., PEREGRINE, D.H., and BULLOCK, G.N. (2009). "Violent breaking wave impacts. Part 2: modelling the effect of air." *Journal of Fluid Mechanics*, Vol. 641, pp. 389-430 (DOI: 10.1017/S0022112009991571).
- CAIN, P., and WOOD, I.R. (1981). "Instrumentation for Aerated Flow on Spillways." *Jl of Hyd. Div.*, ASCE, Vol. 107, HY11, Nov., pp. 1407-1424.
- CHACHEREAU, Y., and CHANSON, H. (2011). "Bubbly Flow Measurements in Hydraulic Jumps with Small Inflow Froude Numbers." *International Journal of Multiphase Flow*, Vol. 37, No. 6, pp. 555-564 (DOI: 10.1016/j.ijmultiphaseflow.2011.03.012).
- CHANSON, H. (1997a). "Air Bubble Entrainment in Free-Surface Turbulent Shear Flows." *Academic Press*, London, UK, 401 pages.
- CHANSON, H. (1997b). "Air Bubble Entrainment in Open Channels. Flow Structure and Bubble Size Distributions." *International Journal of Multiphase Flow*, Vol. 23, No. 1, pp. 193-203 (DOI: 10.1016/S0301-9322(96)00063-8).
- CHANSON, H. (2004a). "The Hydraulics of Open Channel Flow: An Introduction." *Butterworth-Heinemann*, 2nd edition, Oxford, UK, 630 pages (ISBN 978 0 7506 5978 9).
- CHANSON, H. (2004b). "Unsteady Air-Water Flow Measurements in Sudden Open Channel Flows." *Experiments in Fluids*, Vol. 37, No. 6, pp. 899-909 (DOI: 10.1007/s00348-004-0882-3).
- CHANSON, H. (2005). "Air-Water and Momentum Exchanges in Unsteady Surging Waters : an Experimental Study." *Experimental Thermal and Fluid Science*, Vol. 30, No. 1, pp. 37-47 (DOI: 10.1016/j.expthermflusci.2005.03.017).
- CHANSON, H. (2007). "Bubbly Flow Structure in Hydraulic Jump." *European Journal of Mechanics B/Fluids*, Vol. 26, No. 3, pp.367-384 (DOI:10.1016/j.euromechflu.2006.08.001).
- CHANSON, H. (2009a). "The Rumble Sound Generated by a Tidal Bore Event in the Baie du Mont Saint Michel." *Journal of the Acoustical Society of America*, Vol. 125, No. 6, pp. 3561-3568 (DOI: 10.1121/1.3124781).
- CHANSON, H. (2009b). "Current Knowledge In Hydraulic Jumps And Related Phenomena. A Survey of Experimental Results." *European Journal of Mechanics B/Fluids*, Vol. 28, No. 2, pp. 191-210 (DOI: 10.1016/j.euromechflu.2008.06.004).
- CHANSON, H. (2010). "The Underwater Noise of Breaking Tidal Bores in Laboratory." in DOCHERTY, N.J., and CHANSON, H. (2010), "Characterisation of Unsteady Turbulence in Breaking Tidal Bores including the Effects of Bed Roughness." *Hydraulic Model Report No. CH76/10*, School of Civil Engineering, The University of Queensland, Brisbane, Australia, pp. 89-95.
- CHANSON, H. (2011a). "Tidal Bores, Aegir, Eagre, Mascaret, Pororoca: Theory and Observations." *World Scientific*, Singapore, 220 pages (ISBN 9789814335416).

LENG, X., and CHANSON, H. (2019). "Air-Water Interaction and Characteristics in Breaking Bores." *International Journal of Multiphase Flow*, Vol. 120, Paper 103101, 17 pages (DOI: 10.1016/j.ijmultiphaseflow.2019.103101) (ISSN 0301-9322).

- CHANSON, H. (2011b). "Hydraulic Jumps: Turbulence and Air Bubble Entrainment." *Journal La Houille Blanche*, No. 1, pp. 5-16 & Front cover (DOI: 10.1051/lhb/2011026).
- CHANSON, H. (2016a). "Phase-Detection Measurements in Free-Surface Turbulent Shear Flows." *Journal of Geophysics and Engineering*, Vol. 13, No. 2, pp. S74-S87 (DOI: 10.1088/1742-2132/13/2/S74).
- CHANSON, H. (2016b). "Atmospheric Noise of a Breaking Tidal Bore." *Journal of the Acoustical Society of America*, Vol. 139, No. 1, pp. 12-20 (DOI: 10.1121/1.4939113)
- CHANSON, H., AOKI, S., and HOQUE, A. (2006). "Bubble Entrainment and Dispersion in Plunging Jet Flows: Freshwater versus Seawater." *Journal of Coastal Research*, Vol. 22, No. 3, May, pp. 664-677 (DOI:10.2112/03-0112.1).
- CHANSON, H., and TOI, Y.H. (2015). "Physical Modelling of Breaking Tidal Bores: Comparison with Prototype Data." *Journal of Hydraulic Research*, IAHR, Vol. 53, No. 2, pp. 264-273 (DOI: 10.1080/00221686.2014.989458).
- CIPRIANO, R.J., and BLANCHARD, D.C. (1981). "Bubble and Aerosol Spectra Produced by a Laboratory 'Breaking Wave'." *Journal of Geophysical Research*, Vol. 86, No. C9, pp. 8085-8092.
- CLIFT, R., GRACE, J.R., and WEBER, M.E. (1978). *"Bubbles, Drops, and Particles."* Academic Press, San Diego, USA, 380 pages.
- COAKLEY, D.B., HALDEMAN, P.M., MORGAN, D.G., NICOLAS, K.R., PENNDORF, D.R., WETZEL, L.B., and WELLER, C.S. (2001). "Electromagnetic scattering from large steady breaking waves." *Experiments in Fluids*, Vol 30, No. 5, pp. 479-487.
- CUMMINGS, P.D., and CHANSON, H. (1997). "Air Entrainment in the Developing Flow Region of Plunging Jets. Part 1: Theoretical Development." *Journal of Fluids Engineering*, Transactions ASME, Vol. 119, No. 3, pp. 597-602 (DOI: 10.1115/1.2819286).
- DEANE, G.B. (1997). "Sound Generation and Air Entrainment by Breaking Waves in the Surf Zone." *Journal of Acoustical Society of America*, Vol. 102, No. 5, pp. 2671-2689.
- DEANE, G.B., and STOKES, M.D. (2002). "Scale Dependence of Bubble Creation Mechanisms in Breaking Waves." *Nature*, Vol. 418, 22 Aug., pp. 839-844.
- ERVINE, D.A., McKEOGH, E.J., and, ELSAWY, E.M. (1980). "Effect of Turbulence Intensity on the rate of Air Entrainment by Plunging Water Jets." *Proc. Instn Civ. Engrs*, Part 2, June, pp. 425-445.
- GUALTIERI, C., and CHANSON, H. (2010). "Effect of Froude Number on Bubble Clustering in a Hydraulic Jump." *Journal of Hydraulic Research*, IAHR, Vol. 48, No. 4, pp. 504-508 (DOI: 10.1080/00221686.2010.491688).
- HOYT, J.W., and SELLIN, R.H.J. (1989). "Hydraulic Jump as 'Mixing Layer'." *Journal of Hydraulic Engineering*, ASCE, Vol. 115, No. 12, pp. 1607-1614.

LENG, X., and CHANSON, H. (2019). "Air-Water Interaction and Characteristics in Breaking Bores." *International Journal of Multiphase Flow*, Vol. 120, Paper 103101, 17 pages (DOI: 10.1016/j.ijmultiphaseflow.2019.103101) (ISSN 0301-9322).

- HUNT, J.C.R., WRAY, A.A., and MOIN, P. (1998). "Eddies, Streams, and Convergence Zones in Turbulent Flows." *Proceedings of the Summer Program 1998*, Centre for Turbulence Research, pp. 193-208.
- KOCH, C., and CHANSON, H. (2009). "Turbulence Measurements in Positive Surges and Bores." *Journal of Hydraulic Research*, IAHR, Vol. 47, No. 1, pp. 29-40 (DOI: 10.3826/jhr.2009.2954).
- LENG, X., and CHANSON, H. (2015a). "Turbulent Advances of a Breaking Bore: Preliminary Physical Experiments." *Experimental Thermal and Fluid Science*, Vol. 62, pp. 70-77 (DOI: 10.1016/j.expthermflusci.2014.12.002).
- LENG, X., and CHANSON, H. (2015b). "Unsteady Turbulence in Expansion Waves in Rivers and Estuaries: an Experimental Study." *Environmental Fluid Mechanics*, Vol. 15, No. 5, pp. 905-922 (DOI: 10.1007/s10652-014-9385-9).
- LENG, X., and CHANSON, H. (2015c). "Breaking Bore: Physical Observations of Roller Characteristics." *Mechanics Research Communications*, Vol. 65, pp. 24-29 (DOI: 10.1016/j.mechrescom.2015.02.008).
- LENG, X., and CHANSON, H. (2016). "Coupling between Free-surface Fluctuations, Velocity Fluctuations and Turbulent Reynolds Stresses during the Upstream Propagation of Positive Surges, Bores and Compression Waves." *Environmental Fluid Mechanics*, Vol. 16, No. 4, pp. 695-719 & digital appendix (DOI: 10.1007/s10652-015-9438-8).
- LENG, X., and CHANSON, H. (2017a). "Unsteady Velocity Profiling in Bores and Positive Surges." *Flow Measurement and Instrumentation*, Vol. 54, pp. 136-145 (DOI: 10.1016/j.flowmeasinst.2017.01.004).
- LENG, X., and CHANSON, H. (2017b). "Upstream Propagation of Surges and Bores: Free-Surface Observations." *Coastal Engineering Journal*, Vol. 59, No. 1, paper 1750003, 32 pages & 4 videos (DOI: 10.1142/S0578563417500036).
- LENG, X., and CHANSON, H. (2018). "Two-phase Flow Characteristics of a Breaking Tidal Bore Roller: Microscopic Properties." *Hydraulic Model Report No. CH109/18*, School of Civil Engineering, The University of Queensland, Brisbane, Australia, 190 pages (ISBN 978-1-74272-195-8).
- LONGUET-HIGGINS, M.S. (1982). "Parametric Solutions for Breaking Waves." *Jl. of Fluid Mech.*, Vol. 121, pp. 403-424.
- LU, S.S., and WILLMARTH, W.W. (1973). "Measurements of the Structure of the Reynolds Stress in a Turbulent Boundary Layer." *Journal of Fluid Mechanics*, Vol. 60, Part 3, pp. 481-511.
- LUBIN, P., and CHANSON, H. (2017). "Are breaking waves, bores, surges and jumps the same flow?" *Environmental Fluid Mechanics*, Vol. 17, No. 1, pp. 47-77, (DOI: 10.1007/s10652-016-9475-y).

LENG, X., and CHANSON, H. (2019). "Air-Water Interaction and Characteristics in Breaking Bores." *International Journal of Multiphase Flow*, Vol. 120, Paper 103101, 17 pages (DOI: 10.1016/j.ijmultiphaseflow.2019.103101) (ISSN 0301-9322).

- LUBIN, P., GLOCKNER, S., and CHANSON, H. (2010). "Numerical Simulation of a Weak Breaking Tidal Bore." *Mechanics Research Communications*, Vol. 37, No. 1, pp. 119-121 (DOI: 10.1016/j.mechrescom.2009.09.008).
- LUBIN, P., and GLOCKNER, S. (2015). "Numerical simulations of three-dimensional plunging breaking waves: generation and evolution of aerated vortex laments." *Journal of Fluid Mechanics*, Vol. 767, pp. 364-393 (DOI: 10.1017/jfm.2015.62).
- MOUAZE, D., CHANSON, H., and SIMON, B. (2010). "Field Measurements in the Tidal Bore of the Sélune River in the Bay of Mont Saint Michel (September 2010)." *Hydraulic Model Report No. CH81/10*, School of Civil Engineering, The University of Queensland, Brisbane, Australia, 72 pages.
- MURZYN, F., MOUAZE, D., and CHAPLIN, J.R. (2005). "Optical Fibre Probe Measurements of Bubbly Flow in Hydraulic Jumps." *International Journal of Multiphase Flow*, Vol. 31, No. 1, pp. 141-154.
- PEREGRINE, D.H. (2003). "Water wave impact on walls." *Annual Review of Fluid Mechanics*, Vol. 35, pp. 23-43.
- SENE, K.J., HUNT, J.C.R., and THOMAS, N.H. (1994). "The role of coherent structures in bubble transport by turbulent shear flows." *Journal of Fluid Mechanics*, Vol. 259, pp. 219-240.
- SIMPSON, J.H., FISHER, N.R., and WILES, P. (2004). "Reynolds Stress and TKE Production in an Estuary with a Tidal Bore." *Estuarine, Coastal and Shelf Science*, Vol. 60, No. 4, pp. 619-627.
- STOKER, J.J. (1957). "Water Waves. The mathematical Theory with Applications." Interscience Publishers, New York, USA, 567 pages.
- SUN, S., and CHANSON, H. (2013). "Characteristics of Clustered Particles in Skimming Flows on a Stepped Spillway." *Environmental Fluid Mechanics*, Vol. 13, No. 1, pp. 73-87 (DOI: 10.1007/s10652-012-9255-2).
- SUN, S., LENG, X., and CHANSON, H. (2016). "Rapid Operation of a Tainter Gate: Generation Process and Initial Upstream Surge Motion." *Environmental Fluid Mechanics*, Vol. 16, No. 1, pp. 87-100 (DOI: 10.1007/s10652-015-9414-3).
- TOOBY, P.F., WICK, G.L., and ISAACS, J.D. (1977). "The Motion of a Small Sphere in a Rotating Velocity Field: a Possible Mechanism for Suspending Particles in Turbulence." *Journal of Geophysical Research*, Vol. 82, No. 15, pp. 2096-2100.
- TOOMBES, L., and CHANSON, H. (2007). "Surface Waves and Roughness in Self-Aerated Supercritical Flow." *Environmental Fluid Mechanics*, Vol. 7, No. 3, pp. 259-270 (DOI 10.1007/s10652-007-9022-y).
- TRICKER, R.A.R. (1965). "Bores, Breakers, Waves and Wakes." American Elsevier Publ. Co., New York, USA.

- LENG, X., and CHANSON, H. (2019). "Air-Water Interaction and Characteristics in Breaking Bores." *International Journal of Multiphase Flow*, Vol. 120, Paper 103101, 17 pages (DOI: 10.1016/j.ijmultiphaseflow.2019.103101) (ISSN 0301-9322).
- WANG, H. (2014). "Turbulence and Air Entrainment in Hydraulic Jumps." *Ph.D. thesis*, School of Civil Engineering, The University of Queensland, Brisbane, Australia, 341 pages & Digital appendices (DOI: 10.14264/uql.2014.542).
- WANG, H., and CHANSON, H. (2015a). "Air Entrainment and Turbulent Fluctuations in Hydraulic Jumps." *Urban Water Journal*, Vol. 12, No. 6, pp. 502-518 (DOI: 10.1080/1573062X.2013.847464).
- WANG, H., and CHANSON, H. (2015b). "Experimental Study of Turbulent Fluctuations in Hydraulic Jumps." *Journal of Hydraulic Engineering*, ASCE, Vol. 141, No. 7, Paper 04015010, 10 pages (DOI: 10.1061/(ASCE)HY.1943-7900.0001010).
- WANG, H., and CHANSON, H. (2016). "Self-similarity and Scale Effects in Physical Modelling of Hydraulic Jump Roller Dynamics, Air Entrainment and Turbulent Scales." *Environmental Fluid Mechanics*, Vol. 16, No. 6, pp. 1087-1110 (DOI: 10.1007/s10652-016-9466-z).
- WANG, H., HU, Z., and CHANSON, H. (2015). "Two-dimensional bubble clustering in hydraulic jumps." *Experimental Thermal and Fluid Science*, Vol. 68, pp. 711-721 (DOI: 10.1016/j.expthermflusci.2015.07.006).
- WANG, H., LENG, X., and CHANSON, H. (2017). "Bores and Hydraulic Jumps. Environmental and Geophysical Applications." *Engineering and Computational Mechanics*, Proceedings of the Institution of Civil Engineers, UK, Vol. 170, No. EM1, pp. 25-42 (DOI: 10.1680/jenclm.16.00025).
- WOOD, I.R. (1991). "Air Entrainment in Free-Surface Flows." *IAHR Hydraulic Structures Design Manual No. 4*, Hydraulic Design Considerations, Balkema Publ., Rotterdam, The Netherlands, 149 pages.